Measurement of accessible reactive surface area in a sandstone, with application to CO_2 mineralization

Gautier Landrot* [1], Jonathan B. Ajo-Franklin, Li Yang, Stefano Cabrini, and Carl I. Steefel

glandrot@gmail.com, jbajo-franklin@lbl.gov, lyang@lbl.gov, scabrini@lbl.gov, CISteefel@lbl.gov

Lawrence Berkeley National Laboratory, 1 Cyclotron Rd, Berkeley, CA 94720-8099, USA

* Corresponding author: glandrot@gmail.com, tel: +66 90 79 77 922; fax: +66 29 42 81 06

1- Present address: Department of Environmental Engineering, Kasetsart University, 10th floor, Building 14, 50 Ngamwongwan Road, Jatujak, Bangkok, 10900, Thailand.

Abstract

A new characterization approach is employed in this study that enables the measurement of the surface area of each reactive mineral located within the connected pore network of a sandstone from a carbon sequestration pilot site in Cranfield, Mississippi. The mineral distribution is measured in 2D by chemical mapping using Energy Dispersive X-ray Spectroscopy-Scanning Electron Microscopy (SEM-EDX) coupled with an image segmentation technique. The pore structure is mapped at high resolution using a pixel contrast thresholding technique applied to 2D Backscattered Electron Microscopy (BSE-SEM) images. After merging the mineral distribution and porosity maps, the accessibilities of each mineral present in the rock sample are quantified. These quantifications require characterizing in advance the connected pore network in the merged maps, which is done considering the permeability of chlorite measured at the nano-scale in three dimensions by Focus Ion Beam-Scanning Electron Microscopy (FIB-SEM). The accessible surface area of each reactive mineral is finally determined by multiplying the fraction of each reactive mineral next to the connected pore network, measured in 2D, with the surface area of the connected pore network in the rock, which is measured in 3D from X-ray based micro tomography (μ-CT) images and subsequently refined with a correction factor that accounts for the missing pore connectivity. This is necessary since μ-CT voxel resolution (880 nm) is lower than the pixel resolution achieved with BSE-SEM (330 nm). The accessible surface areas of the reactive minerals present in the sandstone rock can be used to accurately scale the rate constants for quantitative prediction and ultimately control of CO_2 injection in the subsurface at the Cranfield pilot site.

Keywords: CO_2 sequestration; reactive surface area; pore connectivity; FIB-SEM; mapping; synchrotron microtomography

1 Introduction

In-situ mineralization of CO_2 in the form of stable carbonate phases in the deep subsurface is potentially a safe and cost-effective technique to store the excess of carbon dioxide in the atmosphere (Bachu, 2000; Oelkers et al., 2008; Bickle, 2009). To optimize this technology, reactive transport models could be used to predict and ultimately control the fate of CO_2 post injection at the carbon sequestration sites. The scaling of the rate constants associated with the reactive minerals that are considered in these types of models, however, depends on the method used to characterize the surface areas of the reactive minerals, since the rate constants are typically normalized to a surface area unit. Mineral surface areas can be estimated based on geometry, which typically assume that all grains in the rock or mineral have similar shape and size. They can be also measured directly with the Brunauer Emmett & Teller (BET) method (Hodson, 2006; Scislewski and Zuddas, 2010). While this approach may give a reasonable estimate in uncemented materials, it works poorly for cemented sediments, or crystalline rock. This is because the pores in a crystalline material are, for the most part, poorly connected, which implies that BET measurement of ground material cannot give a reasonable estimate of the surface area that is actually accessible by transport (Navarre-Sitchler et al., 2009; Navarre-Sitchler et al., 2011). Alternatively, the accessible surface areas of the minerals can be indirectly measured from kinetic experiments (either stirred-cell or plug flow column reactors) using fluid chemical data (Jove et al. 2004, Scislewski and Zuddas, 2010). However, no analytical method currently available can directly measure on a large scale these reactive mineral surfaces on reservoir samples. Although 2D maps obtained by X-ray Fluorescence Spectroscopy, Energy Dispersive X-ray Spectroscopy (EDX), or Electron probe micro-analyzer (EPMA) can be useful in identifying and characterizing the spatial distributions of the mineral phases in direct contact with the pores in rock samples (Tovey and Krinsley, 1991; Michibayashi et al., 1999; Togami et al., 2000; Glassley et al. 2002; Peters, 2009; Prêt et al., 2010a, 2010b; Tsuji et al., 2010), these techniques cannot be employed alone to measure the accessible surface areas of the minerals in 3D. Recent studies have shown that X-ray based μ-tomography (μ-CT) is useful for example in imaging in 3D the connected pore network in porous media (Navarre-Sitchler et al., 2009; Zandomeneghi et al., 2010; Heath et al., 2011), mapping carbonate precipitate

evolution (Armstrong and Ajo-Franklin, 2011), and distinguishing grain types in rock, based on their size and geometry (Pamukcu and Gualda, 2010; Cnuddle et al., 2011), as well as differentiating dense minerals that have high attenuation coefficients from minerals and the air in the pores that have low attenuation coefficients (Gualda et al., 2010). However, since this technique only measures the attenuation of X-rays in 3D in the samples (related to density and z-number), it does not provide direct chemical information, and thus often cannot definitively map the heterogeneous mineral distribution in natural rock samples, although phase identification in simplified porous composites is sometimes possible. Focused Ion Beam coupled with Scanning Electron Microscopy (FIB-SEM) is a relatively new 3D destructive imaging technique that has been so far mostly used for TEM foil preparation (Heaney et al., 2001; Wirth, 2004). This technique can image in 3D a sample with nanometer resolutions while measuring simultaneously its chemical content using an EDX detector. However, FIB-SEM cannot probe within a reasonable time frame a volume that is larger than a few tens of micrometers (Uchic et al., 2007). Therefore, this method is not suitable for measuring in 3D the mineral distribution in a large rock sample.

The goal of this study is to measure the reactive surface areas of the minerals present in a sandstone collected from a carbon sequestration pilot site in Cranfield, Mississippi. The reactive surface areas of the minerals focused in this study are the water-mineral surface areas within the connected pore network, including dead-end pores. As a result, the approach employed does not map preferential fluid flow paths. The discrepancy between laboratory and field rates is a longstanding issue in the Earth Sciences and has severely limited our ability to develop defensible predictive models for the behavior of fluids in the subsurface. This is particularly problematic for the case of geologic storage of CO_2, where it is important to quantify the amount of carbon stored in mineral form. One of the suggestions for explaining this discrepancy is that the rates constants associated with the reactive minerals that are considered in the reactive transport models are often scaled with mineral surface areas that are characterized by BET analyses or geometry calculations. These surface areas account for the total porosity of the minerals, although not all of the pores in the subsurface are accessible to the major flow paths through which the reactive fluids pass. As a consequence, the accessible surface areas measured in this study are more appropriate for use in

reactive transport models that will be developed to predict the fate of CO_2 injected in the subsurface at the Cranfield site than the mineral surfaces measured by BET or estimated by geometry calculations.

Several analytical techniques are employed in this study that probe the sample at different scales and dimensions. The reactive surface areas of the minerals must be measured in a sufficiently large volume of the sample such that a reliable averaging of the entire chemical and physical heterogeneity of the rock is possible. Accordingly, the surface area of the connected pore network was measured in a large volume of the sample by X-ray based micro tomography (μ-CT), at a 0.88 μm voxel resolution. Also, the mineral distribution and pore structure were measured in 2D respectively by EDX and Backscattered Electron Microscopy (BSE) in a large region of the rock. The characterization approach used in this study also integrates data collected by FIB-SEM at high resolution in small volumes of the rock, so that the macropores (larger than 50 nm) and some of the mesopores that are larger than 14 nm, which may be part of the connected pore network, can be also taken into account in the determinations of mineral accessibility. Our characterization approach could be used not only to quantify the accessible reactive surface areas in rock samples, but also to map the physical and chemical modifications undergone at different scales in the media after CO_2 injection. This would be extremely useful in understanding the apparent low extent of mineral trapping that was observed during batch experiments in which a sandstone sample from the Cranfield site, with a chemical composition very similar to our sample, was reacted with CO_2 for a few weeks (Lu et al., 2012).

2 Materials and Methods

2.1 Sampling & bulk characterization

The sandstone sample was extracted from whole core obtained from a depth of 10446 feet below ground surface (3183 meters) at a geologic carbon sequestration pilot site in Cranfield, Mississippi (well CFU 31-F2). The sample was part of the D/E unit of the Lower Tuscaloosa Formation, a quartz rich fluvial sandstone with abundant authigenic chlorite coatings (Lu et al., 2012). No supercritical CO_2 was injected in the rock prior to sampling. Porosity and permeability measurements were performed on the sample, as well as quantitative bulk X-ray Diffraction (XRD) analyses, by Core Laboratories (TX) following their standard "Whole-Rock and Clay Fractions Analytical Procedures". The surface area of the sample was measured by Brunauer-Emmett-Teller (BET) analysis using an Autosorb-1 (Quantachrome Instruments) and krypton as the adsorbate at 77.3 K.

2.2 SEM analysis and data processing

2.2.1 Sample preparation and data acquisition

The rock sample was embedded in a Epotek 301 resin, cut to a ~ 30-50 µm thin slab, and mounted to a SupraSil 3 quartz slide with a cyanocrylate-based adhesive, by Spectrum Petrographics Inc., WA. The thin section was analyzed by a Carl Zeiss EVO MA10 Scanning Electron Microscope (SEM), at the Earth & Planetary Sciences Department, UC Berkeley, CA. Images were taken with a 25 KeV accelerating voltage, a ~ 2.3 A tungsten filament current, a 100 nA beam current, a 30 µm aperture size, and a 12 mm free working distance. Backscattered Electron Microscope (BSE) images, of 3072 x 2304 $pixels^2$ in dimensions and in TIFF format were collected and subsequently thresholded to extract in two dimensions the porosity structure of the rock. Chemical analyses with an Energy Dispersive X-ray Spectroscopy (EDX) detector (EDAX, Inc.) were performed within regions of the sample (i.e. 2D mapping) or specific locations (i.e. discrete analyses), using a ~2 μm^2 spot size. These analyses were carried out with a 4 nA intensity probe current, a total X-ray count above 3000, and a dead time between 20 and 30 %. The EDX

elemental maps of 512 x 400 pixel^2 in dimensions were collected with a 2 µm/pixel resolution and a dwell time of 200 µs. The concentrations of the elements featured in the EDX patterns were not calibrated with standards, which implies that the EDX results reported in this study are not quantitative, but only qualitative. Hence, these results can be useful only in identifying the nature of the elements presents at a given location, but they do not provide accurate concentration values of the measured elements. However, comparisons of the relative abundance of the elements between various samples should be reliable, which implies that the thresholding procedure can still be carried out quantitatively.

The data processing associated with the SEM analyses, described in paragraphs 2.2.2, and the µ–tomography and FIB-SEM analyses, respectively described in paragraphs 2.2.3 and 2.2.4, were carried out using codes written with the programming language software Matlab (V. 7.11.1.866 MathWorks).

2.2.2 Image thresholding

A pixel contrast intensity thresholding technique was employed to extract the porosity structure from BSE image using an approach similar to the one employed by Peters (2009). A contrast intensity value was chosen as a threshold in the BSE image's histogram, which sorts all the pixels of the BSE image based on their respective contrast intensity on a scale from 0 to 255. This threshold value was used to differentiate in Equation (1) regions A and B, which are two groups of pixels in the histogram respectively corresponding to the pores/fractures and minerals mapped in the BSE image. In Equation (1), $I_{\text{region A, region B}}$ refers to the threshold value separating regions A and B, while $N_{\text{region A}}$ and $N_{\text{region B}}$ are the number of pixels in regions A and B, respectively.

$$\frac{1}{N_{\text{region A}}}\left|\frac{dN_{\text{region A}}}{dI_{\text{region A, region B}}}\right| + \frac{1}{N_{\text{region B}}}\left|\frac{dN_{\text{region B}}}{dI_{\text{region A, region B}}}\right| \quad (1)$$

The determination of the threshold required first considering a set of contrast intensity values in the histogram of the BSE image, where the pixels corresponding to the minerals and those corresponding to the pores and fractures

cross each other. The threshold value to be determined is thus one of the contrast intensity values featured in this region of the histogram. The result of Equation (1) was then calculated after separating regions A and B by each contrast intensity featured in this set of values. The desired threshold is the contrast intensity in this group of values that gives the lowest result when calculating Equation (1) (Peters, 2009). All pixels in the BSE image that have a contrast intensity below or equal to this threshold correspond to the pores or fractures of the rock. These pixels are then assigned a "1" to the BSE image that is converted from a grayscale format (with pixel values ranging from 0 to 255) to a binary format (with pixel values equal to 0 or 1). All pixels in the BSE image with a contrast intensity above the threshold value correspond to the minerals present in the rock, and are assigned a "0" value in the processed image. The same pixel contrast intensity thresholding approach was employed in the method described in 3.1.2 to differentiate groups of pixels featured in the histograms associated with EDX elemental maps collected at specific locations or regions in the rock.

2.3 μ-CT analysis and data processing

The rock was cut to a small rectangular volume (8 mm x 3 mm x 3 mm) using a small amount of deionized water to wet the cutting area. The sample was then analyzed for 3D pore-scale structure using synchrotron X-ray μ-tomography at beamline 8.3.2, Advanced Light Source, LBNL, with a 0.88 μm/voxel resolution. Data was acquired in monochromatic imaging mode at 23 keV through use of a wide bandpass multilayer monochromator. X-ray projections were converted into visible light using a 35 micron CsI:Ti scintillator and magnified using a 10X microscope objective (Mitutoyo) before being recorded by a 4008x2762 CCD (Cooke PCO 4000). Recorded projections (1801 per tile) were reconstructed after normalization and denoising using a commercial filtered backprojection algorithm (Dierick et al. 2004). More details concerning the principles of this technique and procedures to reconstruct 3D images of samples analyzed by μ-CT at beamline 8.3.2 are available in previous studies (e.g. Navarre-Sitchler et al., 2009, Armstrong and Ajo-Franklin, 2011).

Each reconstructed μ-CT slice, cropped at the desired dimensions, was processed using the same pixel contrast thresholding approach described in paragraph 2.2.2. After an image of the total pore network was obtained by stacking all the thresholded tomographic slices converted to binary format, a burning algorithm was used to identify the pores connected to each other in 3D. The code assigned a "2" value to the pixels corresponding to the pores (i.e. the pixels with a "1" value) starting from one face of the cube. It then spread inward into the cube by assigning a "2" value to the pixels corresponding to the pores that are located next to those already burnt (i.e. the pixels with a "2" value assigned to them). Only the pore pixels that are linked from one side of the cube to the opposite side were reassigned by the code a value of "1", while the rest of the pixels were assigned a "0" value. After determining the connected pore network in 3D along the three axes of the cube, a "marching cubes" algorithm was employed to draw patches within the connected pore network (Newman and Yi, 2006) using the native isosurface function of Matlab. The surface areas of all patches were then quantified and summed together so as to infer the surface area of the entire connected pore network in $pixel^2$ unit. This surface area was then normalized to the cubic volume dimensions that were considered in these measurements in order to determine the surface area of the connected pore network in $pixel^2/pixel^3$ unit. This latter value was finally converted to units of m^2/g based on the resolution of the μ-CT technique (0.88 μm/voxel) and the mass of the rock volume.

2.4 FIB-SEM analysis and data processing

The small rectangular volume of the rock sample analyzed by μ-CT was also coated with AuPd and subsequently analyzed by Focused Ion Beam- Scanning Electron Microscopy (FIB-SEM) using a Zeiss XB1540 EsB at the Molecular Foundry, LBNL. Scanning electron microscopy imaged the sample with a 5 KeV accelerating voltage, a 5 mm working distance, and a secondary electron detector. The rock sample was milled by a focused ion beam perpendicular to the surface of the rock sample, while tilted from the electron beam by a 53 ° angle. The ion beam was generated by a 30 KeV gallium ionic source constantly maintained at a ~ 2 μA current. The clay region within the sandstone, to be imaged in three dimensions using FIB-SEM, was located in the rock based on clay texture observed

from secondary electron SEM images. After finding a region of interest, a large trench was milled in front of it with the focused ion beam using a 10 nA probe current. The latter was required to sputter quartz, which was quite resistant to the ion beam. A lower current (500 pA) was used to mill a ~ 36 x 13 μm^2 flat surface in the front part of the targeted clay region exposed to the electron beam by the trench. After an image of this surface was taken by the SEM using the secondary electron detector, a built-in image reconstruction function featured in the FIB-SEM software (SmartSEM, ZEISS) was used to correct for the 36 ° angle between the electron beam and the clay surface. The reconstructed image obtained in this fashion was then representative of the mineral surface probed by the electron beam from a 90° angle. The clay surface imaged by the SEM was then sputtered by the FIB using a 500 pA current. A new 36 x 13 um^2 surface, separated from the previous one by 14 nm inside the clay, was then exposed to the electron beam for SEM imaging. These sputtering and imaging steps were cyclically repeated until three hundred SEM images were collected, which were then stacked to obtain a 3D image of the mineral region. The first and last tiles of the 3D volume probed by FIB-SEM were analyzed by SEM-EDX mapping using a ZEISS EVO MA10 SEM featuring an EDX detector (from EDAX, Inc.), at the Earth and Planetary Department, UC Berkeley, CA. The averaged EDX patterns of the collected EDX maps were used to verify that the chemical composition of the probed material is the same at the beginning and end of the FIB-SEM analyses, as well as to verify the identity of the targeted clay.

The data collected with FIB-SEM were processed with the same methods employed with the µ-CT data (paragraph 2.3) to map in 3D the total pore network and measure the surface area of the connected pore network. After extracting the pore structure from each SEM image tile, which were cropped to a 12.6 x 4.21 μm^2 frame, the total porosity was measured by counting the number of black pixels from all three hundred tiles, which was then divided by the total number of pixels in all tiles, and then multiplied by 100 to convert to percent. After applying the burning algorithm to map the connected pores inside the volume, the connected porosity was measured in the volume using the same pixel counting method that was employed to quantify the total porosity.

3 Results & Discussion

3.1 Mapping of the rock in 2D

3.1.1 Porosity maps

Some of the channels inside the clay mineral regions and the fractures inside the quartz, which were observed from BSE images taken at different magnifications, were several tens of micrometers long and about 1 µm wide. These grooves may be part of the connected pore network, given the fact that they seemed to connect different clay regions based on observations from BSE images. To successfully map these channels and fractures, BSE images of 1017 µm x 762 µm in dimensions were collected with a 331 nm/pixel resolution. The porosity structure was not extracted with adequate accuracy by the contrast thresholding technique from BSE images that had a resolution coarser than 331 nm/pixel, since parts of the thin grooves seen in the BSE images were missing in the resulting porosity maps. A resolution of 331 nm/pixel resolution, however, seemed to preserve most of the channels and fractures during the thresholding of the BSE images. Figures 1(a) and 1(b) show one example of a BSE image with a 331 nm/pixel resolution and its corresponding thresholded image, respectively. The entire structures of the thin grooves featured in Figure 1(a) are also observed in Figure 1(b), which suggests that our method successfully extracted the porosity network from the BSE images.

3.1.2 Mineral distribution map

Results from quantitative bulk XRD analyses indicate that the rock is composed of quartz (79 %), chlorite (12 %), kaolinite (3 %), illite/mica (3 %), and mixed layers of illite and smectite (about 2.5 % of illite and 0.5 % of smectite). Energy Dispersive X-Ray Spectroscopy (EDX) analyses were performed at locations in the rock thin section corresponding to specific minerals. These locations were selected from BSE images based on mineral texture

observations, since each mineral present in the rock sample has a specific and recognizable texture in the BSE images. Sets of ten EDX patterns per mineral category, taken at locations corresponding to kaolinite, illite/mica, or chlorite, and reported in Figure 2, consistently represent well the type of clay targeted. For example, Al, Si, and O are the three main elements featured in the ten EDX patterns taken in regions of the rock identified provisionally as corresponding to kaolinite. Since the latter is the only mineral present in the sample that is composed exclusively of these three elements, our results suggest that the EDX technique can successfully identify kaolinite based on its chemical composition. The ten EDX patterns taken in chlorite regions consistently feature much more Fe, and also to a lesser extent Mg, than those taken in the two other types of clay region shown in Figure 2. Finally, the ten EDX patterns taken in illite/mica regions consistently feature more K than those taken in the two other types of clay region shown in Figure 2. This suggests that these mineral categories can be differentiated from each other by the EDX technique. Accordingly, the mineral distribution of the rock was measured in 2D using EDX chemical maps of 1024 x 796 μm^2 dimensions (i.e. similar to the BSE map size), taken at the Si, Al, K, Fe, Ti, and Mg edges, with a 2 µm/pixel resolution (Figure 3 (a)). A set of thresholds was applied to the histogram associated with each EDX elemental map, taking into consideration the chemical composition of all minerals in the rock identified by quantitative bulk XRD. The thresholds t_K, t_{Ti}, t_{Fe}, and t_{Mg} were applied to the histograms associated with the K, Ti, Fe, and Mg elemental maps respectively so as to differentiate two groups of pixels. The first group features pixels that have the lowest intensity contrast values in the histograms, and are homogeneously distributed in the elemental maps (Figure 3 (b)). These pixels were thus identified as those corresponding to the background level of K, Ti, Fe, and Mg in their respective elemental map. The second group features pixels that have contrast intensities values higher than those in the first set, and are distributed within specific regions of the elemental maps. These pixels were thus identified as those corresponding to specific minerals. Two thresholds, t_{Al1}, and t_{Al2}, were applied to the histograms associated with the Al elemental maps to differentiate three groups of pixels (Figure 3 (b)). The first group features pixels that have the lowest contrast values in the histograms, and are homogeneously distributed in the elemental maps. These pixels were thus identified as those corresponding to the background level of Al. The

second group features pixels that have contrast intensity values higher than those featured in the first set, and which are locally distributed in specific clay regions of the elemental maps, except in kaolinite regions. This was observed by comparing the location of each set of pixels in the Al elemental map with mineral textures observed in the BSE maps. The third group features pixels that have contrast intensity values higher than those observed in the first and second sets, and are exclusively distributed in the Al elemental maps at locations corresponding to kaolinite regions based on observations from Al elemental maps and BSE maps. Similarly, two thresholds, $t_{Si1,}$ and $t_{Si2,}$ were applied to the histograms associated with the Si elemental map to differentiate three groups of pixels. The first set features pixels that have the lowest intensity contrast values in the histograms and are locally distributed in the Si elemental maps at regions corresponding to chlorite based on comparisons between the Si elemental maps and BSE images. The second group features pixels with contrast intensity values higher than those in the first group and are also locally distributed in the elemental map, but in other regions between the large quartz grains. The third group features pixels with contrast intensity values higher than those in the first and second groups and are exclusively distributed in the Si elemental maps at locations corresponding to the large quartz grains. Accordingly, a gray pixel representing quartz mineral was displayed at a given location in the mineral distribution map when the pixel contrast intensity value was above t_{Si2} in the Si elemental map and below t_K, t_{Ti}, t_{Fe}, t_{Mg}, t_{Al1}, and t_{Al2} respectively in the K, Ti, Fe, Mg, and Al elemental maps (Figure 3 (a)). A blue pixel representing chlorite was displayed at a given location in the mineral distribution map when the contrast intensity value was below t_{Si1} in the Si elemental map, above t_{Al1} and below t_{Al2} in the Al elemental map, above t_{Mg} in the Mg elemental map, and above t_{Fe} in the Fe elemental map, since chlorite in the rock sample has more Fe and Mg than kaolinite and illite/mica (Figure 2) or illite/smectite and quartz. A red pixel representing Illite/mica was displayed at a given location in the mineral distribution map when the contrast intensity value was above t_{Si1} and below t_{Si2} in the Si elemental map, above t_{Al1} and below t_{Al2} in the Al elemental map, above t_K in the K elemental map, since illite/mica in the rock sample have more K than in kaolinite and chlorite (Figure 2), or illite/smectite and quartz. A yellow pixel representing kaolinite was displayed at a given location in the mineral distribution map when the contrast intensity value was above t_{Si1}

and below t_{Si2} in the Si elemental map, above t_{Al2} in the Al elemental map, and below t_K, t_{Ti}, t_{Fe}, and t_{Mg} respectively in the K, Ti, Fe, and Mg elemental maps. If the threshold conditions to identify kaolinite, chlorite, and illite/mica were not met at a given location, while the contrast intensity value was above t_{Si1} and below t_{Si2} in the Si elemental map, as well as above t_{Al1} and below t_{Al2} in the Al elemental map, a pixel representing illite/smectite was mapped. In that case, a purple pixel was displayed in the inferred mineral distribution map at this location. Although no oxide phase was identified by quantitative bulk XRD analyses in the Cranfield sample, a few locations in the EDX elemental maps only feature Ti and O, or Fe and O. Consequently, Fe and Ti oxide phases were also included in the mineral distribution maps, assuming that their mineral contents in the rock sample are below 1 %. A brown pixel representing iron oxides was displayed in the mineral distribution map when the contrast intensity value was above t_{Fe} and below t_{Si1}, t_{Al1}, t_K, t_{Ti}, and t_{Mg} respectively in the Si, Al, K, Ti, and Mg elemental maps. Finally, a green pixel representing titanium oxides was displayed in the mineral distribution map when the contrast intensity value was above t_{Ti} and below t_{Si1}, t_{Al1}, t_K, t_{Fe}, and t_{Mg} respectively in the Si, Al, K, Fe, and Mg elemental maps. If all minerals present in the rock were not identified by these sets of threshold conditions at a given location, a pixel was mapped with a grey color slightly darker than the one assigned to quartz. This pixel category only represented less than 1 % of all pixels featured in 40 mineral distribution maps obtained from our method and was not further considered in this study as a mineral category.

3.1.3 Map merging

The porosity structure was mapped by BSE with a 331 µm/pixel resolution in a 1017 x 763 μm^2 area of the sample, while the mineral distribution was mapped by EDX with a 2 µm/pixel resolution in a 1024 x 796 μm^2 area. To merge the two types of maps collected at different resolutions in the same region, the first twenty-five vertical pixel strips on the left and right sides of the porosity structure map and the first eight horizontal pixel strips on the top and bottom sides of the mineral distribution maps were cropped. The images obtained by merging the porosity structure and mineral distribution maps were then 967 x 763 μm^2 in size and displayed the porosity with a

331 nm/pixel resolution and the mineral distribution with a 2 μm/pixel resolution (Figure 4). These composite maps were useful in quantifying the fraction of the minerals that are exposed within the connected pore network in 2D (3.4.3) and therefore accessible via transport.

3.2 Minimum representative surface area

The accessible surface area of each mineral present in the Cranfield rock was measured in a region of the sandstone that includes a quartz content similar to that measured in the entire thin section. First, thirty-nine 2.24 mm x 2.83 mm porosity/mineral distribution maps probing the entire thin section area (3 cm x 2 cm) were stitched together. Each of these composite maps was obtained by a method similar to the one described in 3.1, although the porosity structure was mapped using BSE images that had a 0.97 μm/pixel resolution and the mineral distribution was mapped using EDX images that had a 4 μm/pixel resolution. This latter resolution was suitable to map in a reasonable time frame the mineral distribution included in the entire sample thin section. Each of the thirty-nine sets of EDX elemental maps took about one hour to collect. This resolution was also suitable to map by EDX the spatial distribution of the large quartz grains present in the Cranfield sample, which are often larger than 100 μm. However, a 4 μm/pixel resolution is not ideal to map by EDX the clays present in the rock, since these minerals may be found in regions of a few micrometers or less based on observations from BSE images. Therefore, only the quartz content and the porosity structure were mapped from the image representing the entire thin section obtained with the 39 composite tiles stitched together. The quartz content was measured first in the entire sample area (250 mm^2). The sample area was divided into two equal areas (i.e. 125 mm^2) and the quartz content was measured in each of them. The quartz content values measured in the two 125 mm^2 parcels were averaged together and the error margin of this averaging was calculated considering a 95 % confidence interval. Each parcel was again then divided into two parts of equal area. The quartz content values measured in the new sub-parcels were averaged together and the error margin of this averaging was calculated. This step was repeated several times until the minimum parcel area that had a quartz content similar to the one measured in the entire sample thin

section was determined with a margin of error lower than 10 % and a 95 % confidence interval. The results reported in Table 1 indicate that this area is 29 mm^2. Hence, there is a 95 % chance that any region of this size in the rock thin section has a quartz content similar to the one measured in the entire sample i.e. that the quantity of quartz is spatially invariant across this range of length scales. The fractions of the minerals next to the connected pore network reported in section 3.4 were then measured in a 29 mm^2 region randomly chosen in the rock sample thin section.

3.3 Surface area of the connected pore network

The sample was analyzed by X-ray tomography (μ-CT) at beamline 8.3.2 to measure the porosity structure within the sample, which was required in order to quantify the surface area of the connected pore network in the rock. A 3D image representing a 307 x 307 x 307 μm^3 cubic volume of the sample was obtained by assembling 349 reconstructed tomographic slices that were 307 x 307 μm^2 in lateral dimension, with a 0.88 μm distance between each tile. The total number of tiles and tile dimensions were chosen so that the area of one tile multiplied by the total number of tiles is equal to 29 mm^2. This made it possible to correlate the fractions of the minerals next to the connected pore network, measured in 2D in a 29 mm^2 area, with the averaged surface area of the rock's connected pore network, measured in 3D in multiple 307 x 307 x 307 μm^3 volumes (section 3.4.3). Thirty-one of these volumes were randomly chosen in the sample analyzed by μ-CT in order to minimize the error margin associated with the averaged surface area value of the connected pore network. After mapping in 3D the pore network in each of these thirty-one cubes, the connected pore network was extracted from each volume using a burning algorithm and their surface area was measured using a marching cube algorithm (Figure 5). The average mineral-fluid surface area of the connected pore network measured inside the thirty-one volumes was $1.738 \times 10^{-2} \pm 3 \times 10^{-3}$ m^2/g (with a 95 % confidence interval). This is an apparent value that is relative to the resolution of the μ-CT images (0.88 μm/pixel) and does not represent the surface area of the pore network that is entirely accessible to transport in the sample. Indeed, observations from BSE images in 2D revealed that the sample includes thin channels that are several

micrometers long, which may connect different clay regions, and are about 1 μm or less wide. This implies that some of these channels cannot be mapped in the μ-CT reconstructed images, which have a voxel dimension of 0.88 μm. Section 3.4 describes how a correction factor was obtained to refine the apparent surface area of the connected pore network measured with the μ-CT data in order to account for the porosity present at scales below the resolution of the μ-CT.

3.4 Connected pore network and mineral distribution mapping

The correction factor used to refine the apparent surface area of the connected pore network measured in 3D by μ-CT was inferred in 2D by quantifying the amounts of minerals next to the connected pore network from SEM images taken at two different resolutions. First, a resolution similar to the one used to map the pore structure in the reconstructed μ-CT images was used (3.4.1). Second, a higher resolution was used, so that most of the channels and fractures that may be part of the connected pore network could be mapped. By comparing the amounts of minerals next to the connected pore network measured from the SEM maps taken at these two resolutions, the correction factor could be inferred (3.4.3).

3.4.1 Low resolution composite map

The map shown in Figure 6 represents the porosity structure and mineral distribution within a 29 mm^2 region of the sample that was randomly chosen in the rock thin section. This large image consists of 40 composite maps that were stitched together, with each obtained using our method described in 3.1. The resolution of the pore structure featured in these composites maps, originally equal to 331 nm/pixel, was lowered to 993 nm/pixel, so that it was similar to the one used to map the pore structure in the reconstructed μ-CT images. The colors of the eight pixels corresponding to the different mineral categories or pores surrounding each pore pixel found in the composite maps were identified and the number of pixels per color type was quantified in order to determine the dominant color and assign it to the eight pixels. If two colors or more were equally dominant among the eight pixels, this arbitrarily chosen order was followed: gray (quartz) > yellow (kaolinite) > red (illite/mica) > purple

(illite/smectite) > blue (chlorite) > black (pore). The hierarchical importance of the minerals defined in this priority order did not significantly affect the total porosity value measured in the resulting 29 mm^2 large map, which was quantified by normalizing the number of black pixels over the total number of pixels in the map. The total porosity was equal to 9 % with the prioritization described above and also the same value with the opposite ordering, i.e. quartz < kaolinite < illite/mica < illite/smectite < chlorite < pore. A burning algorithm was then applied to the 29 mm^2 large image in order to map in 2D the connected pore network. It started to "burn" the pixels corresponding to pores located on the four edges of 29 mm^2 map, and then spread inward through the image by burning the pore pixels connected to the ones previously burnt, until all the pores within the connected network were mapped. The connected pores mapped in 2D with this approach are shown in a white color in Figure 6. These results suggest that only a small number of the pores are connected to each other in this 2D map. The connected porosity in this image, which was calculated by quantifying the number of white pixels divided by the total number of pixels in the map, is 1 %. The low pore connectivity observed in Figure 6 is partly due to the resolution used to map the pore structure, which is similar to the one employed to map the porosity in the reconstructed μ-CT images. Additionally, the connected pore network was not accurately constrained in the map shown in Figure 6, since the minerals that include nanoscale porosity were not taken into account. To remedy this, the connected porosity of chlorite was investigated by FIB-SEM, since it is the principal mineral found, in addition to quartz, in the Cranfield sample, and because it includes nanopores that can be clearly observed in the BSE images shown in Figure 2 (c).

3.4.2 Chlorite porosity measurements in 3D

To map the distribution of connected nanopores in a randomly chosen chlorite region within the sample, imaging in 3D by FIB-SEM was carried out (Figure 7). Three hundred tiles separated from each other by 14 nm were ablated by the FIB and imaged by the SEM. The chemical compositions of the first and last tiles were analyzed by SEM-EDX and are shown in Figure 7 (d). These SEM-EDX patterns are similar to the ones corresponding to chlorite in Figure 2 (c). Another indication that FIB-SEM was probing the same mineral from the beginning to the

end of the milling is the fact that the same mineral texture was observed in the three hundred tiles, which could be described at the nanoscale as a random stacking of rosettes. This texture is similar to a Fe-rich form of chlorite, chamosite (Ryan and Hillier, 2002), which is likely the principal form of chlorite within the Cranfield sample, since a high content of Fe was systematically measured by SEM-EDX in chlorite regions (Figure 2 c and Figure 7 d). The mapping of the pore structure in one tile collected with FIB-SEM is shown before and after applying the contrast intensity thresholding technique in Figure 7 (c) and 7 (d), respectively. It should be noted that most of the empty space between the chlorite rosettes is well characterized from the SEM image using the thresholding technique. A total porosity of 16 % was measured in the 12.6 x 4.2 x 4.2 μm^3 chlorite volume after applying the thresholding method to the three hundred tiles. The surface area of the connected pore network in this volume, mapped after applying a burning and marching cube algorithms to the thresholded tiles, is shown in Figure 7 (e). Given the size of the 3D image representing the chlorite volume (223.5 μm^3 with a 14 nm/voxel resolution), the density of chamosite (3.2 g/cm^3), and the surface area measured by the marching cube algorithm (2,680,222 $pixels^2$), the apparent surface area of the connected pore network normalized to the weight of the chlorite volume is 2.35 ± .6 m^2/g. This value is consistent with the total surface area of 52 m^2/g for a natural chamosite mineral measured by BET analysis (Sreedhar et al. 2009). Since the connected porosity measured in the volume was 9 %, more than half of the pores present in the chlorite region are connected to each other, which suggests that the mineral reasonably has connected porosity at the nanoscale. It should be noted in figure 7 (e) that each side of the chlorite volume probed by FIB-SEM is connected to its opposite side by pore channels. One must also take into account that the thresholding technique used to map the pore structure from the FIB-SEM tiles only considers the pore pixels that have contrast intensities well below those of the chlorite pixels. This implies that the deepest holes observed in the SEM images are mapped, but not the shallowest ones, which may have pixel contrast intensities similar to those of the chlorite pixels. This approach thus avoids erroneously mapping some of the chlorite mineral pixels as pores, which would have the effect of introducing artifacts in the porosity measurements. This also implies that the porosity value measured with this method is apparent, although our approach appears to map the majority of the

pores observed in the FIB-SEM tiles (Figure 7 c and Figure 7 d). It is thus possible that the actual total porosity and connected porosity values that account for all pore connectivity in chlorite are higher than those reported in this study.

Another chlorite region found at a different location in the sample than the one discussed above was milled by the FIB. A flat 20 x 10 μm^2 section was sputtered in this chlorite region and exposed to the SEM for imaging after milling a large trench in front of it. The total porosity measured from the SEM image of this flat section of the chlorite region, which was mapped by a contrast intensity thresholding method, was 17%. This value is thus similar to the one measured in the chlorite region probed in 3D. Additionally, the mineral texture observed in this other region was also identical to the one shown in Figure 7 (b). This type of texture is also consistent with those observed at the micro-scale from BSE images in chlorite regions, which exhibit a high porosity (Figure 2 (c)). Therefore, one can reasonably assume that all chlorite minerals in the rock sample are physically similar to the chlorite region probed in 3D by FIB-SEM in this study, and thus include connected nanoporosity.

3.4.3 Accessible mineral surface area quantification

The mineral distribution and pore structure were mapped again in 2D in the 29 mm^2 region of the sample thin section using an approach similar to the one described in 3.4.1, but without lowering the resolution from 331 nm/pixel to 993 nm/pixel. With this approach, most of the long thin channels and fractures observed in the SEM-BSE images can be mapped (Figure 8). The connected pore network was also mapped in this region by assuming that the pore space within the chlorite is 100 % connected. The total number of pixels for each mineral and the numbers of pixels at the mineral/pore interface in Figure 8 were quantified and are reported in Table 2. The total porosity measured from the map using this approach is 15 %, which is similar to the porosity measured in the bulk sample (16 %). This indicates that the analytical approach employed in this study makes it possible to map most of the pores that contribute to the total porosity of the rock. The connected porosity is 12 %, which suggests that most of the pores are connected to each other in the sample. The interface between the minerals and the

connected pore network corresponds to 4,376,102 pixels in this map, while it is equal to only 205,419 pixels in the map shown in Figure 6. Hence, mapping the pore structure at a high resolution and considering the permeability of chlorite increases the extent of the connected pore network by a factor of 21. A more realistic value of the surface area of the connected pore network inside the rock measured in (3.3) is then 21 * 1.738 x 10^{-2} ± 3 x 10^{-3} m^2/g = 0.365 ± 3 x 10^{-3} m^2/g. The fraction of each mineral located next to the connected pore network and the inferred accessible surface area of each mineral in the rock sample are reported in Table 2. The individual accessible surface area reported in Table 2 were obtained by multiplying the accessible fraction of each mineral (Table 2) with the surface area of the connected pore network measured in 3D and refined with the correction factor (i.e. 3.65 x 10^{-1} m^2/g). The accessible surface area of chlorite reported in Table 2 depends on the resolution used to map the porosity structure in Figure 8 and represents the fraction of the clay surface that is exposed to the connected pore network measured in the 29 mm^2 region (shown in white color in Figure 8). The fraction of the chlorite surface next to the connected pore channels inside the clay, which can be imaged at the nanoscale in 3D but cannot be mapped in a 2D mineral distribution image, was also quantified in the map shown in Figure 8 using the results obtained by FIB-SEM. The surface area of the connected pore network inside a 2 x 2 x 2 μm^3 volume of chlorite is 1.88 x 10^{-11} m^2, since it is 5.25 x 10^{-10} m^2 in a 223.5 μm^3 volume, based on the results reported in 3.4.2. Knowing that 12,410,653 turquoise-blue pixels of 2 x 2 um^2 in dimensions, which represent the reactive fraction of chlorite, were quantified in the 29 mm^2 map shown in Figure 8, the surface area inside chlorite accessible via transport in a 29 mm^2 x 2 µm volume is 2.33 x 10^{-4} m^2, or, considering the density of chamosite, 1.26 ± .34 m^2/g. By adding this value to the one reported in Table 2, the total accessible surface area of chlorite in the rock is 1.26 ± .34 m^2/g + 0,116 m^2/g = 1.38 ± .34 m^2/g.

The reactive surface area of this chlorite was measured with a resolution that could image the mesopores larger than 14 nm inside the clay, while the accessible surface areas of the other minerals were measured with a resolution that can only image the pores larger than 331 nm. This latter resolution is high enough to map the reactive surface area of quartz, iron and titanium oxides, since these minerals are observed in the BSE

images in regions that seem to be relatively compact and do not systematically exhibit nanoporosity. The resolution of 331 nm is not sufficient, however, to detect smaller scale features on the mineral surfaces (i.e., nanoscale surface roughness), although this might be estimated by comparing geometric and BET surface areas (Noiriel et al., in review). The sum of the mineral surface areas measured by our multi-technique approach is 1.6 m^2/g, while the BET surface area of a 502 mm^3 uncrushed sample is 4.2 m^2/g. This difference in surface area values may indicate that our method indeed cannot entirely map the nanoscale surface roughness featured in the rock. In addition, the lower surface area value obtained with our method compared to the one measured by BET could be due to the clays other than chlorite in the Cranfield sample featuring connected pore channels that are narrower than 331 nm. This would imply that the accessible surface area values of these minerals would be higher than those reported in this study. However, they still would not be as high as the reactive surface area of chlorite, since the amount of this mineral in the rock is greater than the amounts of the other clays summed together based on quantitative bulk-XRD analyses and the percentages of the minerals measured in the map shown in Figure 8 and reported in Table 2.

The error margin of the accessible surface area values reported in Table 2 is $\pm$ 3 x 10^{-3} m^2/g and is essentially the error margin associated with the surface area quantification in 3D of the connected pore network with the μ-CT data. Collecting multiple composite maps covering several 29 mm^2 regions in the rock was not possible from a practical point of view, given the time required to obtain one composite map and the availability of the SEM device. Therefore, since multiple 29 mm^2 maps were not probed, the error margins associated with the measurements of the surface area refinement factor and the fractions of the minerals located next to the connected pore network could not be determined. Our experimental approach appears to faithfully map the mineral distribution and the pore structure, however, since the amounts of minerals and pores mapped in the 29 mm^2 region determined in this study are similar to those measured by quantitative bulk XRD and porosity analyses respectively. Consequently, it is likely that if the surface area correction factor and the fractions of the minerals located next to the connected pore network were measured in multiple 29 mm^2 regions of the rock, they would be similar to the values reported in this study. This would imply that the error margin associated with the

measurements of these parameters would be low and would not significantly affect the inferred error margin of the reactive surface area values reported in Table 2. The total accessible surface area of chlorite has a high error margin (about 50 %), which is due to the error margin associated with the measurement of the connected surface area of the pore structure inside the clay by FIB-SEM. This error margin may be reduced by averaging the surface areas of the connected pore channels inside chlorite measured at multiple locations in the rock. These surface area values should be similar to each other, since the texture of chlorite appears to be remarkably homogeneous in this particular Cranfield sample based on observations from SEM images, although variations do exist at other locations in the lower Tuscaloosa (see Lu et al. 2012).

The reactive surface area of chlorite is considerably higher than those of the other minerals, even when the large error margins associated with all of these values are considered. This indicates that chlorite is by far the mineral that is most accessible with respect to CO_2 in the rock sample. This must be taken into account when predicting the fate of carbon dioxide in the subsurface at Cranfield, since the chlorite can serve as a source of Fe^{2+}, which can promote the formation of secondary phases such as siderite and ankerite. Results from batch experiments performed over a few weeks on a sandstone from the Cranfield site that had a chemical composition very similar to our rock sample suggested that chlorite is not rapidly dissolved by CO_2 (Lu et al. 2012). It should be noted that our study says nothing immediately about the bulk reactivity of the chlorite, since the intrinsic rate of reaction under supercritical CO_2 conditions needs to be factored in. In addition, while our study indicates that the nanoporosity developed in the chlorite found at Cranfield is connected, this by itself does not yield an effective diffusion rate through this nanoporous chlorite. In other words, there is still a potential for diffusion-controlled reaction, which would have the effect of slowing the overall rate of reaction of the chlorite. In addition, the conclusions about the lack of reactivity of the chlorite in the Lu et al. (2012) study are based primarily on the fact that Mg concentrations do not rise, but it is also possible that secondary Mg-bearing phases may form in the rock, especially in nanoscale microenvironments where the pH may increase locally. Similar experiments should be carried out to study on longer time scales the kinetics and mechanisms of the possible reactions involving chlorite

and CO_2 in the sample, which would be useful in determining if mineral trapping is a viable option to sequester CO_2 at the Cranfield site.

4 Conclusions

We have demonstrated that the characterization approach employed in this study is suitable for mapping the mineral distribution and pore structure found in a reservoir sandstone currently being considered as a CO_2 sequestration site. A suite of techniques were used to probe the sample at scales that range from nm to mm and multiple spatial dimensions in order to address the wide range of pore sizes and the heterogeneous mineral distribution in the rock. The measurement of the connected pore network inside the rock, which directly determines the availability of the minerals for reaction with CO_2, had to be carried out with sub-micron resolution so that the nanoscale connected porosity within the minerals could be taken into account and the thin channels and fractures that may link different clay regions in the sandstone could be quantified. The porosity that was imaged in 3D with the μ-CT technique at a resolution of about a micron was apparent and had to be refined by other means in order to account for all the pores present in the sample. This correction step could be avoided in the near future by quantifying directly at the nanoscale the porosity of the bulk rock with the Small Angle Neutron Scattering (SANS) and Ultra Small Angle Neutron Scattering (USANS) techniques (Melnichenko et al., 2012). The characterization approach used in this study to measure the accessible surface area of each mineral present in the sample, which would be helpful in developing accurate reactive transport models of CO_2 in porous media, could be also employed to characterize the physical and chemical properties of the rock after CO_2 injection. This would be useful in determining where precisely carbon dioxide is trapped in the rock and in identifying the CO_2 sequestration mechanisms.

Acknowledgments

The authors thank Kevin G. Knauss and Andrew Mei for assistance in sample preparation. This research was supported by the Center for Nanoscale Control of Geologic CO_2, an Energy Frontier Research Center funded by the U.S. Department of Energy, Office of Science, Office of Basic Energy Sciences under Award Number DE-AC02-05CH11231. Additional funding was provided by the Office of Basic Energy Sciences through the Geoscience Program, Office of Chemical Sciences, Department of Energy. Samples were provided by the Southeast Regional Carbon Sequestration Partnership (SECARB) Early Test at Cranfield, conducted by the Bureau of Economic Geology, University of Texas at Austin and supported by the U.S. Department of Energy (DOE) National Energy Technology Laboratory (NETL) under Grant Number DE-FC26-05NT42590 to Southern States Energy Board. Synchrotron microtomography was performed with the assistance of Alastair MacDowell and Dula Parkinson at the Advanced Light Source, Beamline 8.3.2, which is supported by the Office of Science, Office of Basic Energy Sciences, of the U.S. DOE (contract DE-AC02-05CH11231). FIB/SEM work was performed at the Nanofabrication Facility within the Molecular Foundry (LBNL) which is supported by the Office of Science, Office of Basic Energy Sciences, of the U.S. DOE (contract DE-AC02—05CH11231).

References

Armstrong, R., Ajo-Franklin, J.B., 2011. Investigating biomineralization using synchrotron based X-ray computed microtomography. Geophys. Res. Lett. 38, L08406

Bachu, S., 2000. Sequestration of CO_2 in geological media: criteria and approach for site selection in response to climate change. Energy Convers. Manag. 41, 953-970

Bickle, M., 2009. Geological carbon storage. Nat. Geosci. 2, 815-818

Cnuddle, V., Boone, M., Dewanckele, J., Dierick, M., Van Hoorebeke, L., Jacobs, P., 2011. 3D characterization of sandstone by means of X-ray computed tomography. Geosphere 7(1), 54-61

Dierick, M., Masschaele, B., Van Hoorebeke, L., 2004. Octopus, a fast and user-friendly tomographic reconstruction package developed in LabView. Meas. Sci. Technol. 15, 1366-1370

Glassley, W.E., Simmons, A.M., Kercher, J.R., 2002. Mineralogical heterogeneity in fractured, porous media and its representation in reactive transport models. Appl. Geochem. 17, 699-708

Gualda, G., Pamukcu, A., Clairborne, L., Rivers, M., 2010. Quantitative 3D petrography using X-ray based tomography: documenting accessory phases with differential absorption tomography. Geosphere 6 (6), 782-792

Heaney, P., Vicenzi, E., Giannuzzi, L., Livi, K.J.T., 2001. Focused ion beam milling: A method of site-specific sample extraction for microanalysis of Earth and planetary materials. Am. Mineral. 86, 1094-1099

Heath, J., Dewers, T., McPherson, B., Petrusak, R., Chidsey, T., Rinehart, A., Mozley, P., 2011. Pore networks in continental and marine mudstones: characteristics and controls on sealing behaviors. Geosphere 7 (2), 429-454

Hodson, M., 2006. Does reactive surface area depend on grain size? Results from pH 3, 25 C far-from-equilibrium flow-through dissolution experiments on anorthite and biotite. Geochim. Cosmochim. Acta 70, 1655-1667

Jove, C. F., Oelkers, E.H., Schott, J., 2004. An experimental study of porosity, reactive surface area and permeability evolution during the dissolution of the Fontainebleau sandstone. Geochim. Cosmochim. Acta 68, 805-817

Lu, J., Kharaka, Y., Thordsen, J., Horita, J., Karamalidis, A., Griffith, C., Hakala, J., Ambats, G., Cole, D., Phelps, T., Manning, N., Cook, P., Hovorka, S.D., 2012. CO_2–rock–brine interactions in Lower Tuscaloosa Formation at Cranfield CO2 sequestration site, Mississippi, U.S.A. Chem. Geol. 291, 269-277

Melnichenko, Y.B., He, L., Sakurovs, R., Kholodenko, A.L., Blach, T., Mastalerz, M., Radlinski, A.P., Cheng, G., Mildner, D., 2012. Accessibility of pores in coal to methane and carbon dioxide. Fuel 91, 200-208

Michibayashi, K., Togami, S., Takano, M., Kumazawa, T., Kageyama, T., 1999. Application of scanning X-ray analytical microscope to the petrographic characterization of a ductile shear zone: an alternative method to image microstructures. Tectonophysics 310 (1999), 55-67

Navarre-Sitchler, A., Steefel, C.I., Sak, P.B. and Brantley, S.L., 2011. A predictive model for weathering rind formation on basalt, Geochim. Cosmochim. Acta 75, 7644-7667

Navarre-Sitchler, A., Steefel, C., Yang, L., Tomutsa, L., Brantley, S., 2009. Evolution of porosity and diffusivity associated with chemical weathering of a basalt clast. J. Geophys. Res., 114, F02016

Newman, T., Li, H., 2006. A survey of the marching cubes algorithm. Comput. Graph. 30, 854-879.

Noiriel, C.; Steefel, C.I., Yang, L., Ajo-Franklin, J., 2011. Upscaling calcium carbonate precipitation rates from pore to continuum scale, Chem. Geol. (in review)

Oelkers, E., Gislason S., Matter J., 2008. Mineral Carbonation of CO_2. Elements 4, 333-337

Pamukcu, A., Gualda, G., 2010. Qualitative 3D petrography using X-ray tomography 2: Combining information at various resolutions. Geosphere 6 (6), 775-781

Peters, C., 2009. Accessibilities of reactive minerals in consolidated sedimentary rock: An imaging study of three sandstones. Chem. Geol. 265, 198-208

Prêt, D., Sammartino, S., Beaufort, D., Fialin, M., Sardini, P., Cosenza, P., Meunier, A., 2010b. A new method for quantitative petrography based on image processing of chemical element maps: Part II. Semi-quantitative porosity maps superimposed on mineral maps. Am. Mineral. 95, 1389-1398

Prêt, D., Sammartino, S., Beaufort, Meunier, A., D., Fialin, M., Michot, L.J., 2010a. A new method for quantitative petrography based on image processing of chemical element maps: Part I. Mineral mapping applied to compacted bentonites. Am. Mineral. 95, 1379-1388

Ryan, P.C., Hillier, S., 2002. Berthierine/chamosite, corrensite, and discrete chlorite from evolved verdine and evaporite-associated facies in the Jurassic Sundance Formation, Wyoming. Am. Mineral. 87, 1607-1615

Scislewski, A., Zuddas, P., 2010. Estimation of reactive mineral surface area during water–rock interaction using fluid chemical data. Geochim. Cosmochim. Acta 4, 6996-7007

Sreedhar, B., Arundhathi, R., Amarnath Reddy, M., Parthasarathy, G., 2009. Highly efficient heterogenous catalyst for acylation of alcohols and amines using natural ferrous chamosite. App. Clay Sci. 43, 425-434

Togami, S., Takano, M., Kumazawa, M., 2000. An Algorithm for the transformation of XRF images into mineral-distribution maps. Can. Mineral. 38, 1283-1294

Tovey, N.K., Krinsley, D.H., 1991. Mineralogical mapping of scanning electron micrographs. Sediment Geol. 75 (1991), 109-123

Tsuji, T., Yamaguchi, H., Ishii, T., Matsuoka, T., 2010. Mineral classification from quantitative X-ray maps using neural network: Application to volcanic rocks. Isl. Arc 19, 105-119

Uchic, M., Holzer, L., Inkson, B., Principe, E., Munroe, P., 2007. Three-dimensional microstructural characterization using focused ion beam tomography. Mrs Bull. 32, 408-416

Wirth, R., 2004. Focused ion beam (FIB): A novel technology for advanced application of micro- and nanoanalysis in geosciences and applied mineralogy. Eur. J. Mineral. 16, 863-876

Zandomeneghi, D., Voltolini, M., Mancini, L., Brun, F., Dreossi, D., Polacci, M., 2010. Quantitative analysis of X-ray microtomography images of geomaterials: application to volcanic rocks. Geosphere 6 (6), 793-804

area (mm^2)	quartz amount (%)	error margin (c.i. 95%)	# of tiles per area	averaged set of tiles
285 *(entire slide surface)*	81.5	± 0.9	39	1
139	81.6	± 1.3	19	2
95	81.5	± 1.6	13	3
44	81.5	± 2.6	6	6
29	81.0	± 3.7	4	9
22	81.5	± 6.1	3	13

Table 1 Amounts of quartz measured in areas of different sizes in the rock. These quantities were used to determine a minimum representative surface area of the rock.

	quartz	chlorite	kaolinite	illite/mica	illite/smectite	Fe oxide	Ti oxide
total number of pixels	142560722	14353187	3058158	7045744	4100746	1808375	349339
number of pixels at the mineral/connected pore interface	3649663	2962630	494405	1028661	662420	471760	38045
total amount (in %)	82.3	8.3	1.8	4.1	2.4	1.0	0.2
accessible fraction (in %)	39.2	31.8	5.3	11.1	7.1	5.1	0.4
reactive surface area (10^{-2} m^2/g)	14.31 ± .3	11.62 ± .3	1.94 ± .3	4.03 ± .3	2.6 ± .3	1.85 ± .3	0.15 ± .3

Table 2 Pixel numbers of the minerals and the mineral/connected pore network interface, total mineral amounts, and fractions of the minerals next to the connected pore network quantified from the map shown in Figure 8. The reactive surface area values for each mineral inferred from these measurements are also reported.

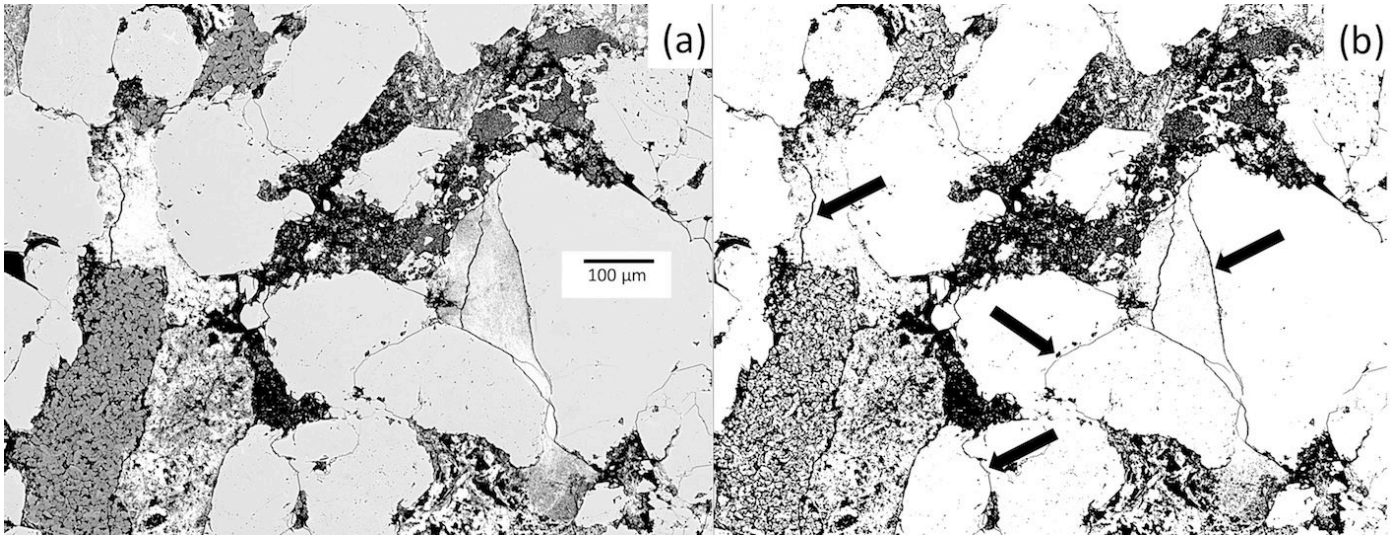

Figure 1 (a) Example of a 1017 µm x 762 µm BSE image with a 331 nm/pixel resolution. (b) Resulting porosity map obtained after applying to the BSE image a contrast intensity thresholding technique. The arrows indicate examples of long thin channels or fractures that were successfully mapped by the thresholding method. These channels seem to connect different clay regions in the rock.

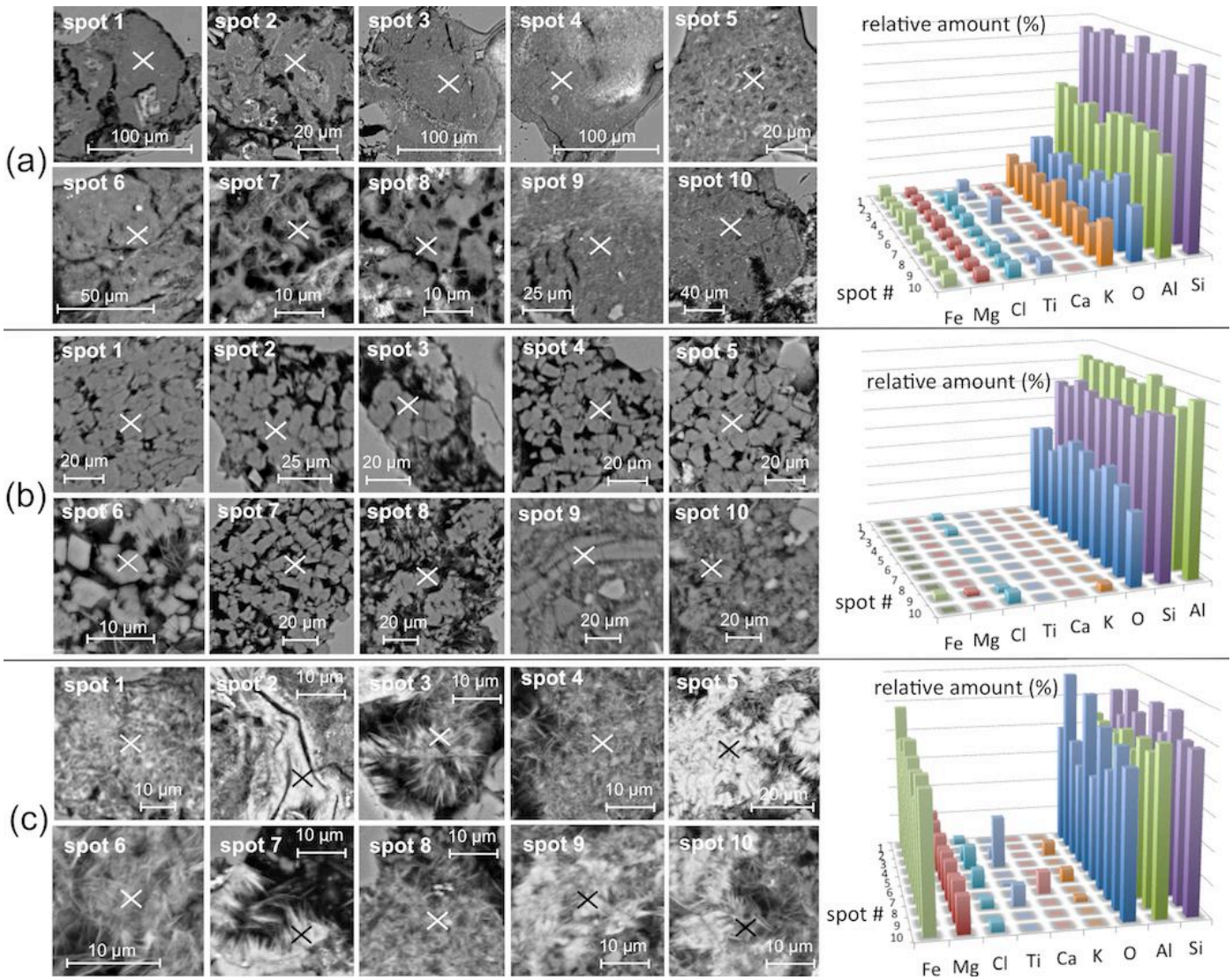

Figure 2 Backscattered Electron Microscopy (BSE) images taken at ten different locations in the rock, and EDX elemental integrated peak areas representing the chemical composition featured at each cross displayed in the BSE images, for (a) illite/mica regions, (b) kaolinite regions, and (c) chlorite regions.

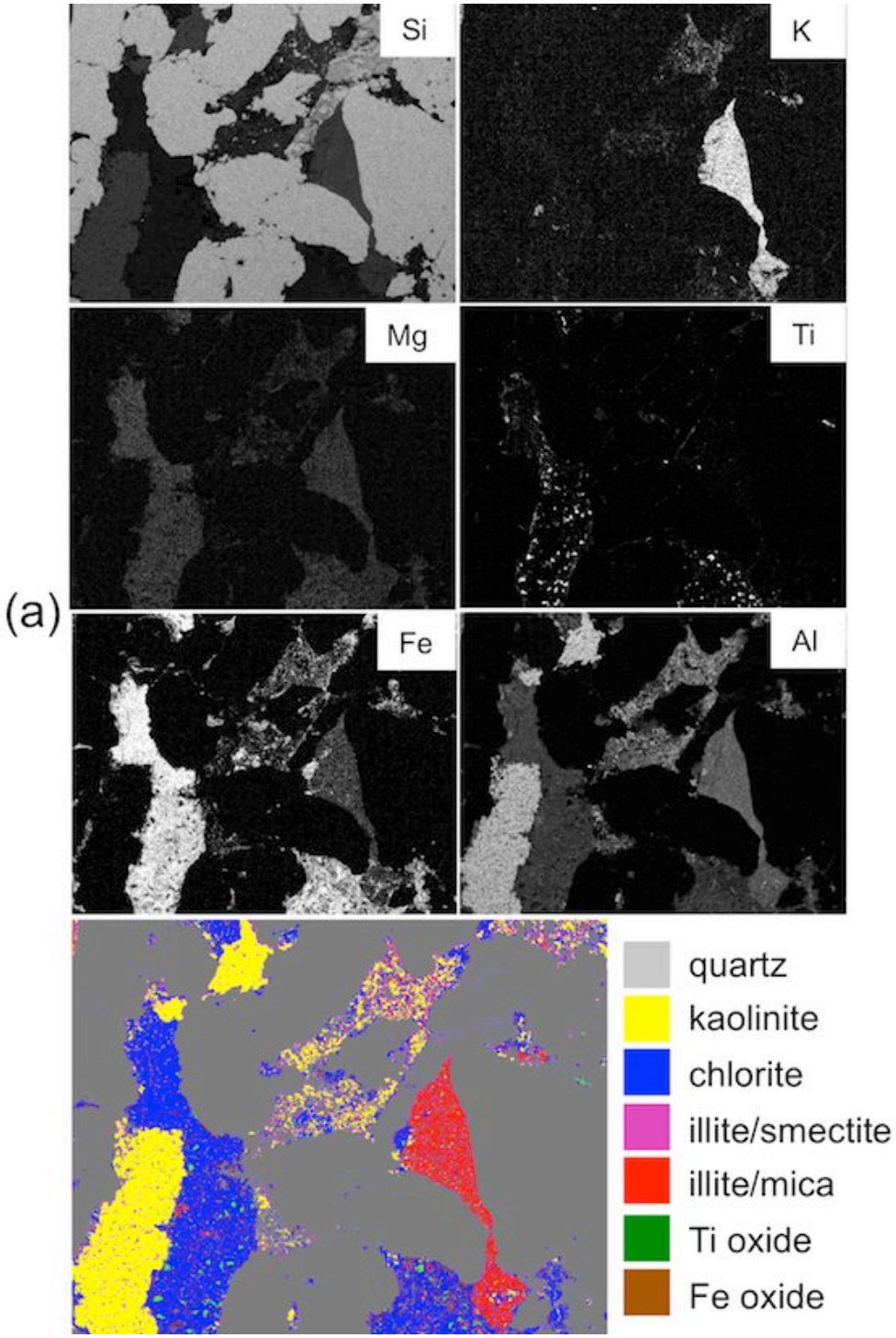

Figure 3 (a) Example of EDX elemental maps and the inferred mineral distribution map. (b) Histograms respectively associated with the Al elemental map and Fe elemental map. One threshold is defined in the Fe histogram (same for the K, Mg, and Ti histograms, not shown), while two thresholds are defined in the Al histogram (same for the Si histogram, not shown).

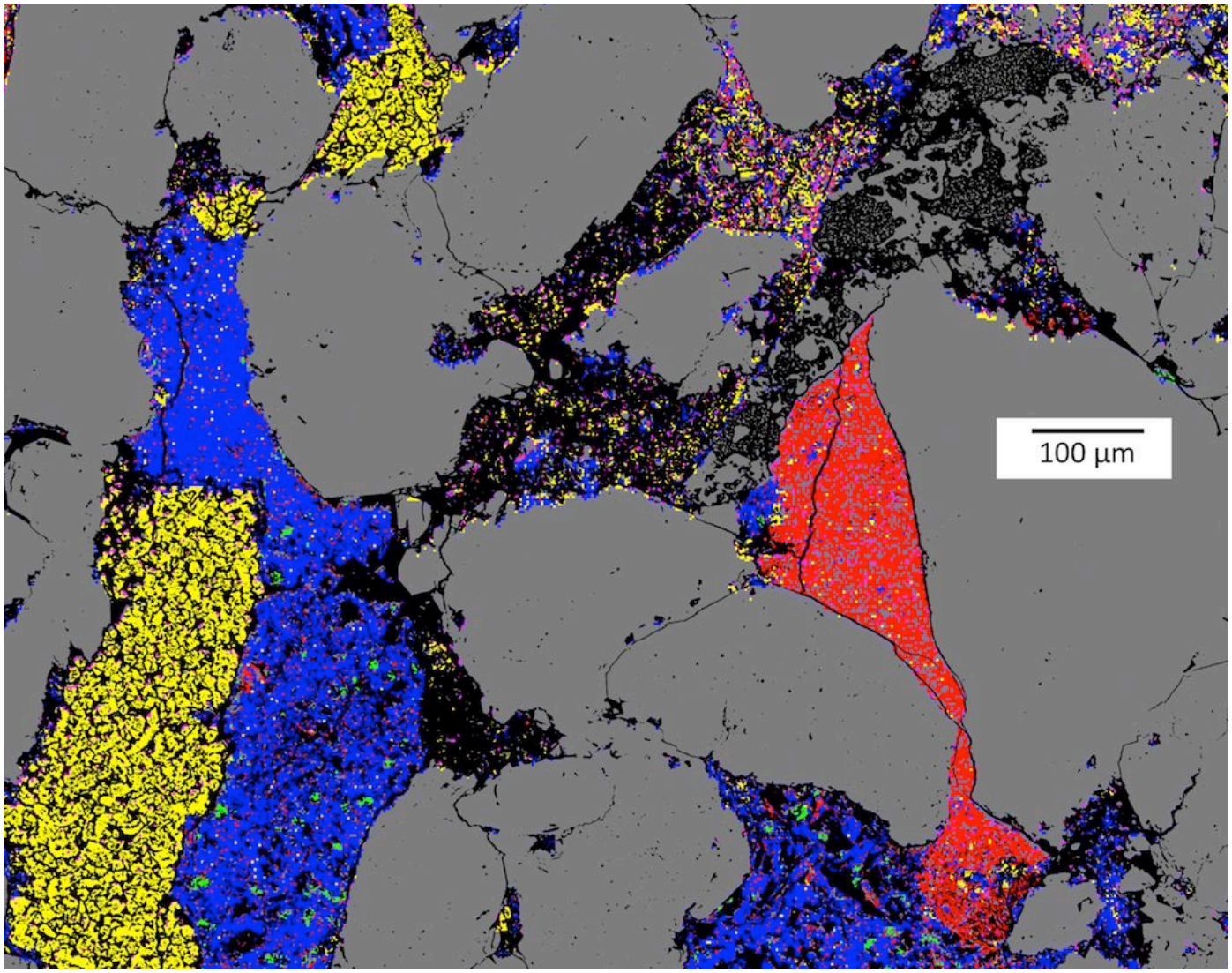

Figure 4 Example of a composite map, consisting of a porosity map merged to a mineral distribution map.

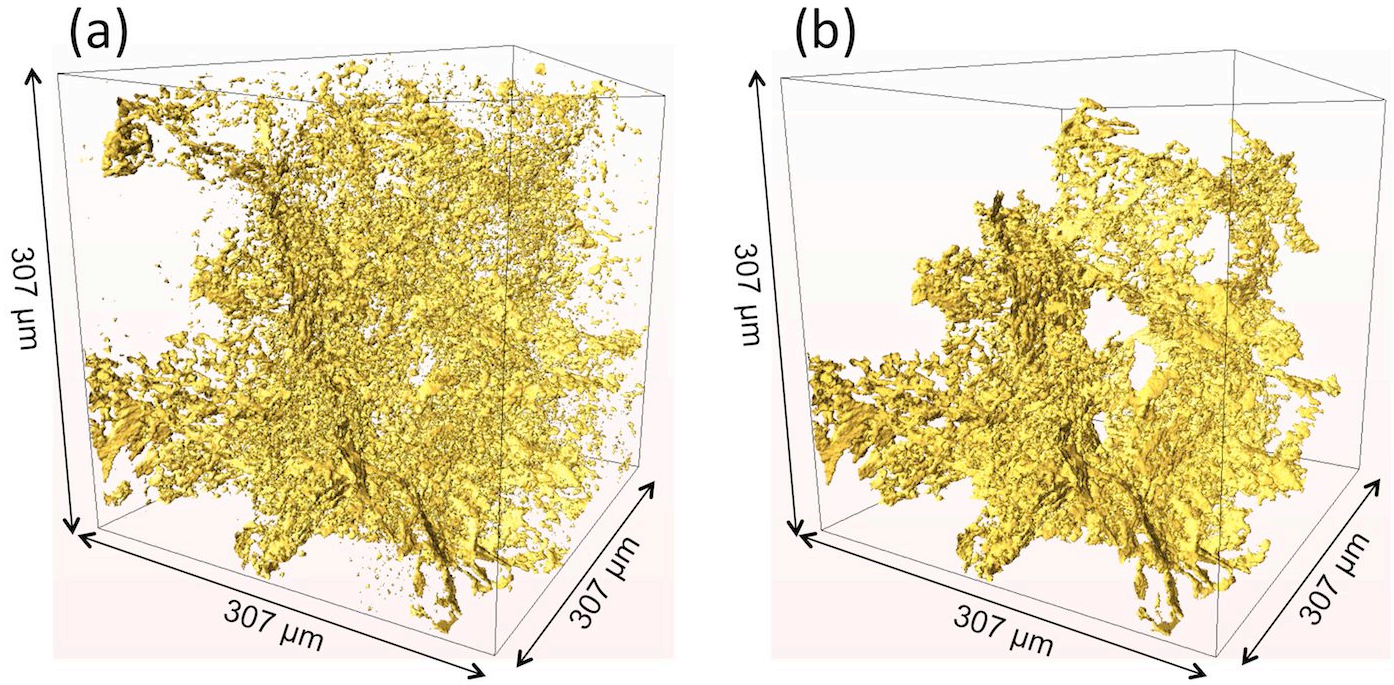

Figure 5 (a) Total apparent surface area and (b) connected apparent surface area of the pore structure in a 307 x 307 x 307 μm^3 volume of the rock.

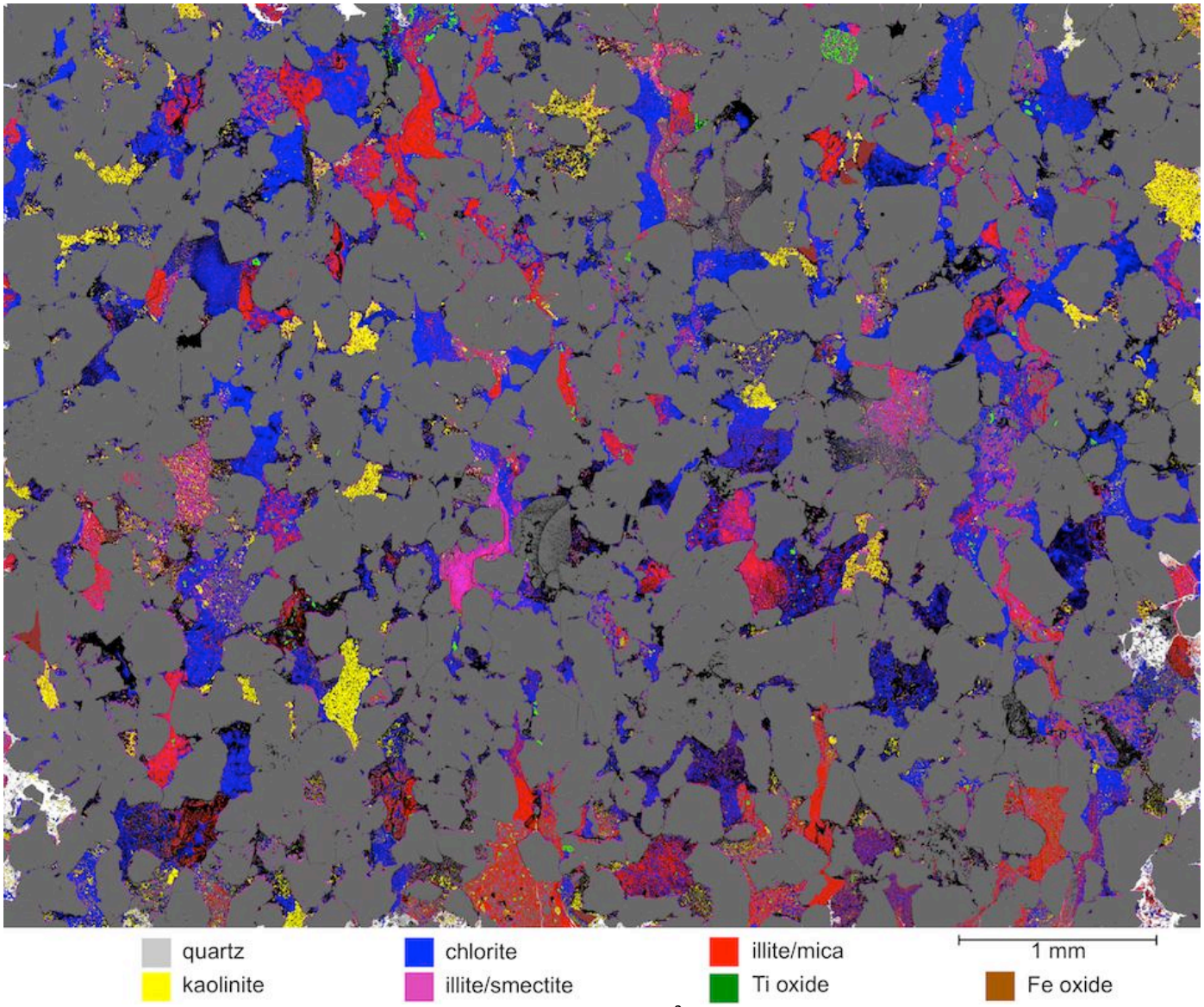

Figure 6 Connected porosity mapping in a 29 mm^2 region of the rock. The porosity is mapped with a resolution similar to the one used to map the pore structure in the reconstructed μ-CT images. The white color represents the connected pore network that starts from the edges of the image and propagates inward.

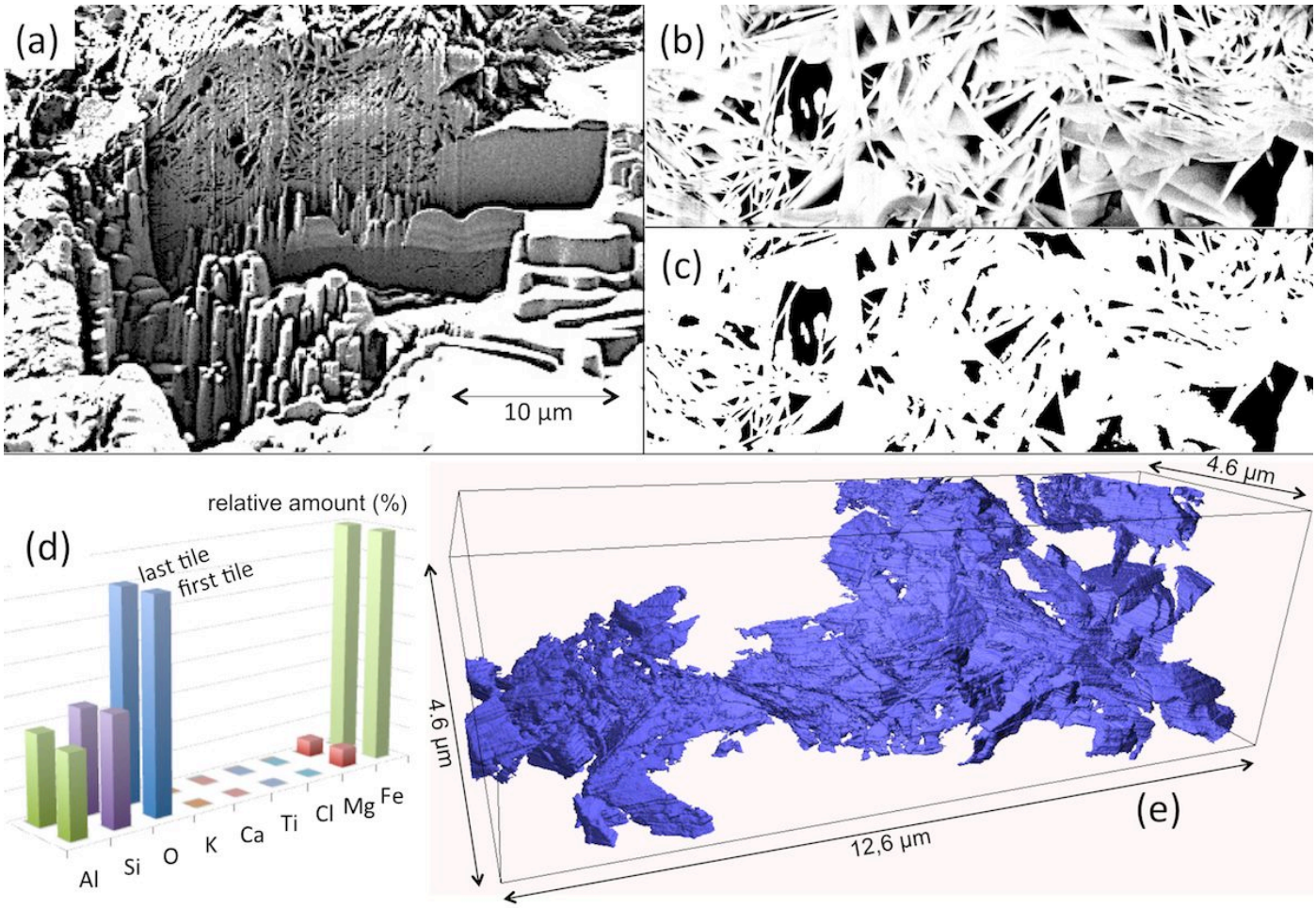

Figure 7 (a) A chlorite region probed by FIB-SEM in the Cranfield sample. A flat section of this region was exposed to the SEM for imaging after a large trench was milled in front of it by the FIB. (b) Secondary Electron (SE) Image representing one 12.6 x 4.2 μm^2 tile cut by the FIB in the chlorite region. (c) SE Image processed by a pixel contrast intensity thresholding technique and converted to a binary format. (d) EDX integrated peak areas representing the chemical compositions of the first tile and last tile milled and imaged by FIB-SEM in a chlorite region. (e) 3D image of the connected pore network featured in a chlorite region probed with FIB-SEM.

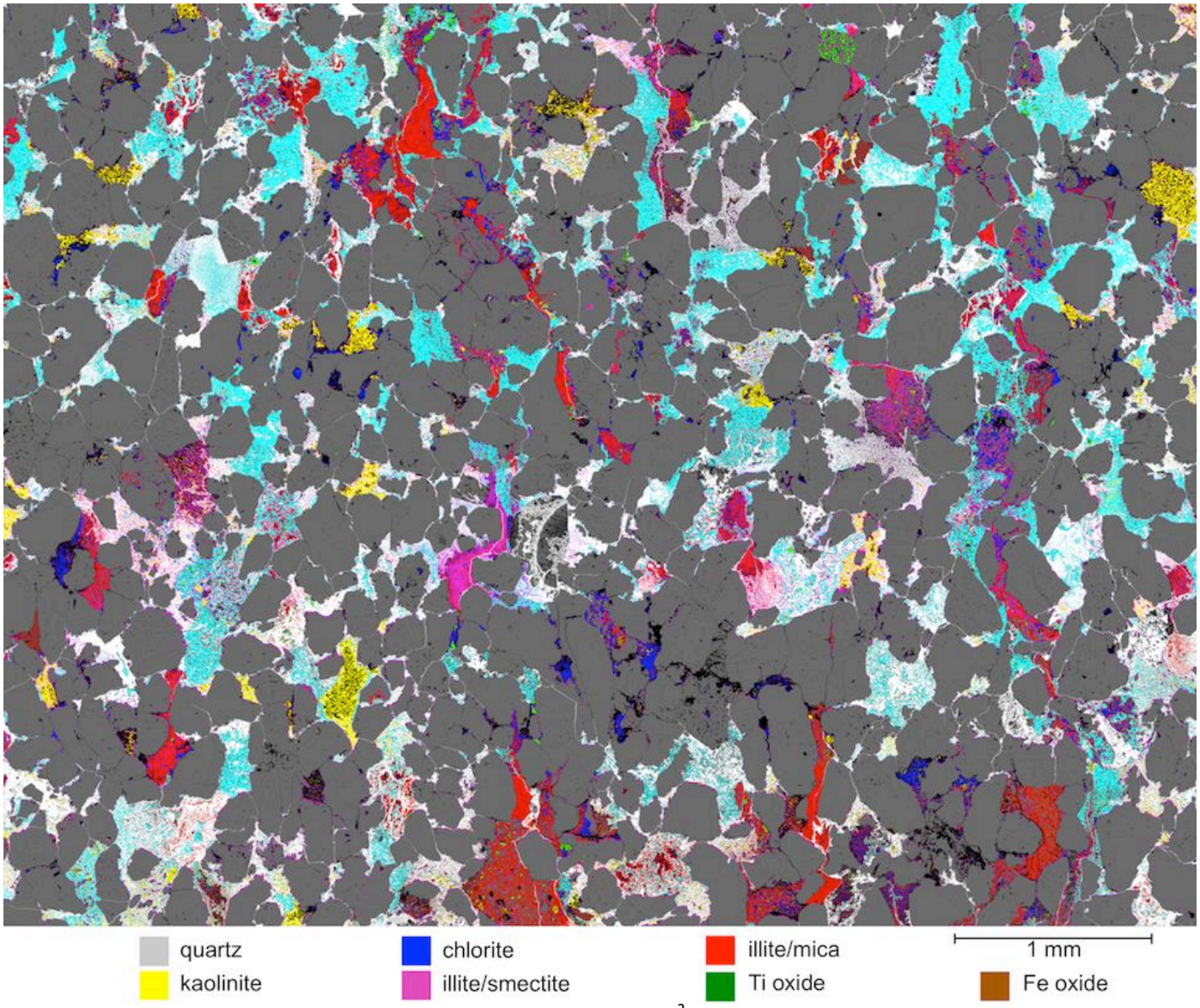

Figure 8 Connected porosity mapping in a 29 mm^2 region of the rock, considering the nanoporosity within chlorite as 100% connected. The porosity is mapped with a 331 nm/pixel resolution. The white color represents the connected pore network that starts from the edges of the image and propagates inward through the map, and the turquoise-blue color represents the chlorite fraction that is linked to the connected pore network measured in the 29 mm^2 region.